TU Delft

Delft University of Technology

Unconventional application of serrated trailing edges for quieter propeller drones

Candeloro, Paolo; Ragni, D.; Pagliaroli, Tiziano

DOI
10.2514/6.2024-3107

Publication date
2024

Document Version
Final published version

Published in
30th AIAA/CEAS Aeroacoustics Conference (2024)

Citation (APA)
Candeloro, P., Ragni, D., & Pagliaroli, T. (2024). Unconventional application of serrated trailing edges for quieter propeller drones. In *30th AIAA/CEAS Aeroacoustics Conference (2024)* Article AIAA 2024-3107 (30th AIAA/CEAS Aeroacoustics Conference, 2024). https://doi.org/10.2514/6.2024-3107

Important note
To cite this publication, please use the final published version (if applicable).
Please check the document version above.

Copyright
Other than for strictly personal use, it is not permitted to download, forward or distribute the text or part of it, without the consent of the author(s) and/or copyright holder(s), unless the work is under an open content license such as Creative Commons.

Takedown policy
Please contact us and provide details if you believe this document breaches copyrights.
We will remove access to the work immediately and investigate your claim.

This work is downloaded from Delft University of Technology.
For technical reasons the number of authors shown on this cover page is limited to a maximum of 10.

Green Open Access added to TU Delft Institutional Repository

'You share, we take care!' - Taverne project

https://www.openaccess.nl/en/you-share-we-take-care

Otherwise as indicated in the copyright section: the publisher is the copyright holder of this work and the author uses the Dutch legislation to make this work public.

Aeroacoustics Conferences
June 4-7, 2024, Rome, Italy
30th AIAA/CEAS Aeroacoustics Conference (2024)

10.2514/6.2024-3107

Check for updates

Unconventional application of serrated trailing edges for quieter propeller drones

Paolo Candeloro *
Engineering Department, Universitá degli Studi Niccoló Cusano, Via Don Carlo Gnocchi 3, 00166 Rome, Italy

Daniele Ragni†
Flow Physics and Technology Department, Faculty of Aerospace Engineering, Delft University of Technology, Kluyverweg 1, 2629HS, The Netherlands

Tiziano Pagliaroli‡
Engineering Department, Universitá degli Studi Niccoló Cusano, Via Don Carlo Gnocchi 3, 00166 Rome, Italy

This article presents an experimental investigation into the use of serrations to reduce propeller trailing edge noise. The study aims to demonstrate the potential of serrated drone blades in reducing tonal noise components while concurrently influencing the broadband noise components in the acoustic spectrum. A series of propellers was designed, manufactured, and tested to establish a relationship between serration geometry and noise mitigation. Subsequently, an aerodynamic and aeroacoustic characterization was performed using load cells, microphone arrays, and Particle Image Velocimetry measurements in an anechoic wind tunnel facility. The results suggest that a proper design of serration geometry can lead to a significant reduction in both tonal and broadband noise components, with the main drawback being a loss in thrust coefficient. Additionally, serrated trailing edge propellers promote enhanced diffusion of peak vorticity in the tip-vortex region, potentially reducing the noise produced by the interaction of the propeller tip-vortex and the surrounding drone structures. Finally, the breakdown of the fluid dynamic correlation length is observed, leading to the reduction of broadband noise.

Downloaded by Technische Universiteit Delft on July 17, 2024 | http://arc.aiaa.org | DOI: 10.2514/6.2024-3107

I. Nomenclature

A	=	amplitude of oscillation
a	=	cylinder diameter
C_p	=	pressure coefficient
Cx	=	force coefficient in the x direction
Cy	=	force coefficient in the y direction
c	=	chord
dt	=	time step
Fx	=	X component of the resultant pressure force acting on the vehicle
Fy	=	Y component of the resultant pressure force acting on the vehicle
f, g	=	generic functions
h	=	height
i	=	time index during navigation
j	=	waypoint index
K	=	trailing-edge (TE) nondimensional angular deflection rate

II. Introduction

DRONES, commonly referred to as Unmanned Aerial Vehicle (UAV), Unmanned Aerial Systems (UAS), or Micro Aerial Vehicle (MAV), are autonomous aircraft characterized by high maneuverability in both hovering and cruise

*Research Fellow, Engineering Department, paolo.candeloro@unicusano.it.
†Associate Professor, Flow Physics and Technology Department, d.ragni@tudelft.nl.
‡Associate Professor, Engineering Department, tiziano.pagliaroli@unicusano.it.

Copyright © 2024 by the American Institute of Aeronautics and Astronautics, Inc. All rights reserved.

operations and user-friendly flight controllability. Such unique properties are attributed to their propulsive system, as these vehicles are typically equipped with single-rotor open systems that operate with high efficiency. UAVs are earmarked to transform the marketplace of deliveries and civil urban transports, speeding up delivery times and reducing costs. The global drone market, according to the reports of Drone Industry Insight, amounted to $\sim$ 14.1 billion $ in 2018 with the prospect of growing by almost 3 times in 2025 [1], such growth is expected despite pandemic issues. Just to give an overview, in the USA there were 1.32 million UAS registered for leisure purposes and 0.385 million for professional applications in 2019 and these numbers are expected to increase by 12% to 1.48 million for the former applications and 115% up to 0.83 million for the latter in 2024 [2, 3]. In the context of the drone market, the overarching strategic goals encompass enhancing endurance and minimizing acoustic emissions. To achieve these objectives, it is imperative to gain comprehensive insights into the noise generation mechanisms and their effects on aerodynamics. This knowledge is a key aspect of the widespread adoption and future design of drones.

Regarding propeller-driven aircraft, the main noise sources are the engine and the propeller itself, and this problem strongly affects the low Reynolds regime too. Therefore, to reduce drone noise signature, the only way to proceed is to optimize both components at the same time. Concerning the engine, generally, MAVs are equipped with electric brushless motors, which significantly reduce the mechanical noise signature ([4–6]). Moreover, the reduction of propeller noise requires particular attention in the design process, since an improvement from an acoustic point of view will be associated with a loss in terms of propulsive force generation. In this manuscript, to mitigate the noise of small propeller serration applied to the trailing edge is employed with a focus on understanding how this affects aerodynamics. Such a control strategy is already present for wind turbines with promising results. In the last few years, the reduction of noise from the propulsive system of small rotors has been the subject of several works in literature: [4, 5, 7–14] represent just a few examples. While several previous works focused on relatively high Reynolds numbers propellers, few studies have focused on low-Reynolds small-scale propellers. For the latter kind of propeller where a considerable area of the rotor is subjected to stall and self-interaction with its slipstream, the effect of the flow features, such as recirculation bubbles, stall cells, and non-uniform boundary layer transition, are exacerbated, and not negligible. For more detail about the noise sources see Candeloro et al.[15, 16]. The use of serrations to reduce propeller noise has been abundantly investigated in the literature. Serrations applied to the TE of an airfoil induce a destructive interference of the pressure fluctuations produced by the flow structures convecting along the slanted edge resulting in a lower noise emission, such result is achieved at the cost of a noticeable reduction in thrust. This strategy is already employed on wind turbine blades and fixed-wing airfoils [17–19]. Nevertheless, a few studies have been devoted to small-scale serrated propellers, therefore an in-depth study is essential to assess the applicability of the strategy.

The use of serrations for wind turbine applications is investigated by Chong et al. [20] and Avallone et al [21]; the former, based on [20, 22], pointed out that significant noise reduction can be achieved if two conditions are met. The first is that the serration length is of the same order as the turbulent boundary layer thickness δ near the TE. The second is that the serration angle (called α in Fig.1) is small, favoring a sharp sawtooth. In addition, Avallone et al. [21] find out that noise reduction depends on frequency. Once a critical value of the Strouhal number was reached no noise reduction was observed. Furthermore, Pang et al.[23] involved an experimental analysis of pitch angle and trailing edge serration effects for serrated small-scale propellers demonstrating that sawtooth serrations employed at the TE can noticeably suppress high-frequency broad-band noise in the far-field. The main drawback observed is that the tonal component seems to increase in the low-frequency region. Moreover, Intravartolo et al.[24] investigate the serration depth effect and demonstrate that an increase in serration depth produces a reduction in the intensity of the trailing edge wake. Nevertheless, if serration depth reaches a value comparable to half of the Mean Aerodynamic Chord (MAC), no further gain in aeroacoustic effect can be observed. Such results are consistent with [6, 25] that proved a sensible mitigation in the noise radiated by the TE associated with a damping in the tails of the Probability Density Function (PDF) was observed. Finally, Halimi et al. [26, 27] provide a mathematical model with the purpose of estimating the broadband noise spectrum of mini-drone in order to quantify the achievable noise reduction due to sawtooth trailing/leading edge. The results show that a noise reduction in the low and mid-frequency region can be obtained, which is, however, associated with an increase in noise at high frequencies.

Downloaded by Technische Universiteit Delft on July 17, 2024 | http://arc.aiaa.org | DOI: 10.2514/6.2024-3107

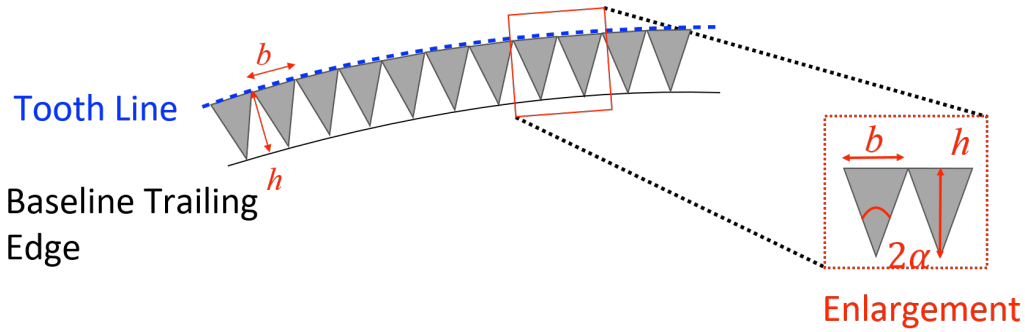

Fig. 1 Representation of the serrated trailing edge. In the enlargement the main geometrical parameters of the tooth are reported: tooth basis b, height h, and the serration angle α.

Downloaded by Technische Universiteit Delft on July 17, 2024 | http://arc.aiaa.org | DOI: 10.2514/6.2024-3107

III. Theoretical Background

A. Noise in Drones: Noise Decomposition

Generally, the propeller aerodynamic noise is split into two main components: tonal and broad-band contributions [6, 8, 24, 25, 28]:

$$p'(\mathbf{x},t) = p'_{TN}(\mathbf{x},t) + p'_{BB}(\mathbf{x},t) \tag{1}$$

where $p'_{TN}(\mathbf{x},t)$ is the tonal component of pressure fluctuations, whereas $p'_{BB}(\mathbf{x},t)$ is the broad-band counterpart. The tonal component is associated with the periodic motion of the blade in the surrounding fluid. Therefore, its frequency and magnitude are directly linked to the rotational velocity. Specifically, for thin blades and low Mach numbers ($M < 1$), this component has primarily two contributions: one sound source related to the blade thickness, p'_T, and one related to the aerodynamic loading, p'_L.

$$p'_{NB}(\mathbf{x},t) = p'_T(\mathbf{x},t) + p'_L(\mathbf{x},t) \tag{2}$$

The thickness term takes into account the fluid displacement due to the body, while the loading counterpart takes count of the unsteady force distribution over the body surface.

On the other hand, the broad-band component is emitted as a result of the interaction between turbulent flow structures and the blade edge. Consequently, it is generated either at the blade's leading/trailing edge or at the blade tip. Generally, it is produced by three main sources: *i)* noise associated with the turbulence of the incoming flow (LE noise); *ii)* noise produced by the interaction of the turbulent boundary layer over the blade surface with the trailing edge (TE noise); and *iii)* noise generated by the potential separation of the flow (Separation noise). [8]. Therefore, the broad-band contribution is commonly divided as:

$$p'_{BB}(\mathbf{x},t) = p'_{TE}(\mathbf{x},t) + p'_{LE}(\mathbf{x},t) + p'_S(\mathbf{x},t) \tag{3}$$

where $p'_{TE}(\mathbf{x},t)$ represents the trailing edge component, p'_{LE} represents the leading edge component, and p'_S represents the term due to the separation. Several authors have already addressed the prediction of trailing edge broad-band noise. A relation between the Power Spectral Density of the trailing noise, S^{TE}_{pp}, and the spanwise velocity correlation length, l_y, is reported in [8] as:

$$S^{TE}_{pp}(r,\theta,\omega) = \frac{B}{8\pi}\left(\frac{\omega c}{2ar}\right)^2 \Delta R\, D(\theta,\phi)\, |I|^2\, \Phi_{pp} l_y \tag{4}$$

where r is the observer position vector, $\omega = 2\pi f$ is the angular frequency, f is the rotational frequency, B is the number of the blades, c is the chord, a is the speed of sound, ΔR is the spanwise length of the blade, $D(\theta,\varphi)$ is the directivity function, I is the radiation integral function, the operator $|\,|^2$ is the square of the absolute value and Φ_{pp} is the wall power spectral density of the pressure fluctuations. There are different models for S^{TE}_{pp} estimation, *e.g.* the one proposed by Schklinker and Amiet [29], or the more recent one proposed by Rozenberg et al. [30], which takes into account the effect of the adverse pressure gradient. On the other hand, l_y is usually evaluated by means of the Corcos' model [31]. The examined noise control strategy, described subsequently, relies on the model proposed in Eq. 4. To be more precise, given that $S^{TE}_{pp} \sim l_y$, a substantial decrease in l_y achieved through variations in the trailing edge (TE) geometry is expected to result in a reduction of noise in the far field.

B. Noise in Drones: Serrated Trailing Edge Propellers

The application of serrations to the TE of the airfoil leads to a reduction in noise generation due to the disruptive interference caused by pressure fluctuations from flow structures along the slanted edge. This technique is currently employed in wind turbine blades and airfoils, as evidenced by studies conducted by Oerlemans [18, 19] and Llorente [17]. However, limited research has been conducted on the implementation of serrations in small rotors. Through a comprehensive review based on existing knowledge of serrations, Ning et al. [32] identified three crucial parameters to ensure the effective use of serrations for noise reduction. The parameters considered are: *i)* the dimensionless tooth height $h^* = h/2\delta$;*ii)* the tooth Aspect Ratio $AR_t = 2b/h$;*iii)* the Strouhal number $St_\delta = f\delta/U$. In this discussion, h and b represent the height and base of the sawtooth pattern, respectively, as illustrated in Fig.1, δ is the boundary layer thickness, f denotes sound frequency, and U_{rel} is the relative velocity. Ning emphasized that for effective noise reduction, h^* should exceed 0.25; otherwise, the serration amplitude is too small. Additionally, the inclination angle α must not exceed 45°, ensuring $AR_t < 4$. Finally, the Strouhal number must overcome 1 for substantial noise reduction, as stated by Howe [22]. Results demonstrate that Serrated Trailing Edges (STE) effectively reduce broadband noise in the high-frequency range without compromising aerodynamic performance. However, in the low-frequency region, the generated noise remains nearly unchanged. The aforementioned criteria serve as the initial guidelines in this manuscript for generating various propellers with integrated serrations, as reported in Sec. IV.A.

IV. Experimental setup

A. Design of the serrated propellers

A baseline propeller, specifically the APC $9 \times 4e$ type was chosen for the experimental campaign, were manufactured to create various test cases, resulting in a total of 23 propellers. This propeller has a diameter of $D = 228.6$ mm and a pitch of 4 degrees. All blades were made by removing material from the TE of the baseline as represented in Fig.1. In addition, a further parameter has been considered: the number of teeth n. Thus, for each geometry considered two propellers have been realized, one with $n = 10$ and one with $n = 5$. In the design of serration geometries, the base b of the serration was varied between 3 and 6 mm, and the height h between 3 and 8 mm; to comply with the constraint $AR_t < 4$ defined in Sec.III.A.

B. Experimental Setup

The initial phase of the study, consisting of an acoustic characterization, was performed in the anechoic chamber of Niccolò Cusano University, that has 3x1.6x3 m in size. The propellers are driven by a brushless motor AXI 2204 and controlled by an Electronic Speed Controller (ESC) Hobbywing Skywalker 20A. Pressure fluctuations were sampled by using Microphone Gefell M360 and National Instrument ACQ board type NI cDAQ-9174. The microphones present a free-field SPL that ranges from 30 to 135 dB, a diameter of 1/4 inch, and a frequency range between 20 Hz and 20 kHz. All pressure signals are acquired for 10 s at sampling frequency $f_s = 51200\,Hz$. The microphone was installed on a manual rotation stage which allowed to vary the polar angle θ in the polar range from $-90°$ to $60°$, covering from the suction side to the wake region of the propellerto perform directivity analysis. The microphone was located within the near field, at a radial distance from the propeller disk $r = 460$ mm $= 2$ D. This choice was made to capture the effects of the STE on hydrodynamic pressure fluctuations in the slipstream. The experimental setup and the polar reference system adopted are sketched in Fig.2(a).

Thereafter, the aerodynamic, aeroacoustic, and fluid-dynamic characterization was performed at the TUDelft University of Technology. The experimental tests were carried out in the A-Tunnel, a vertical, open-jet wind tunnel, where the surrounding of the nozzle exit consists of an anechoic chamber as represented in Fig 2(b). For this study, the exit nozzle is circular with a diameter of 0.60 m. The low cut-off frequency of the anechoic chamber is about 200 Hz.

The propeller is connected to a profiled aluminum nacelle for minimum interference with the propeller flow, the instrumentation (composed of a motor, an encoder, a load cell, and a torque cell) is embedded in the nacelle. The nacelle is supported by stiffened hollow aluminum NACA0012 profiles of 60 mm chord. Nacelle and vertical support are used as cable routing of the power supply, cables for encoder and load cells, and even motor control signals. The entire structure is held up above the nozzle of the tunnel by 4 steel-wire tubes of 20 mm diameter fixed to the tunnel to avoid vibrations. The propeller is driven by an electric brushless motor Leopard Hobby 3536-5T 1520 KV with a diameter of 27.8 mm and a maximum power of 550 W. The motor is powered by a Delta Elektronika DC power supply with a voltage range of 0 - 15 V and a current range of 0 - 100 A. The motor rotational speed is measured by means of

Downloaded by Technische Universiteit Delft on July 17, 2024 | http://arc.aiaa.org | DOI: 10.2514/6.2024-3107

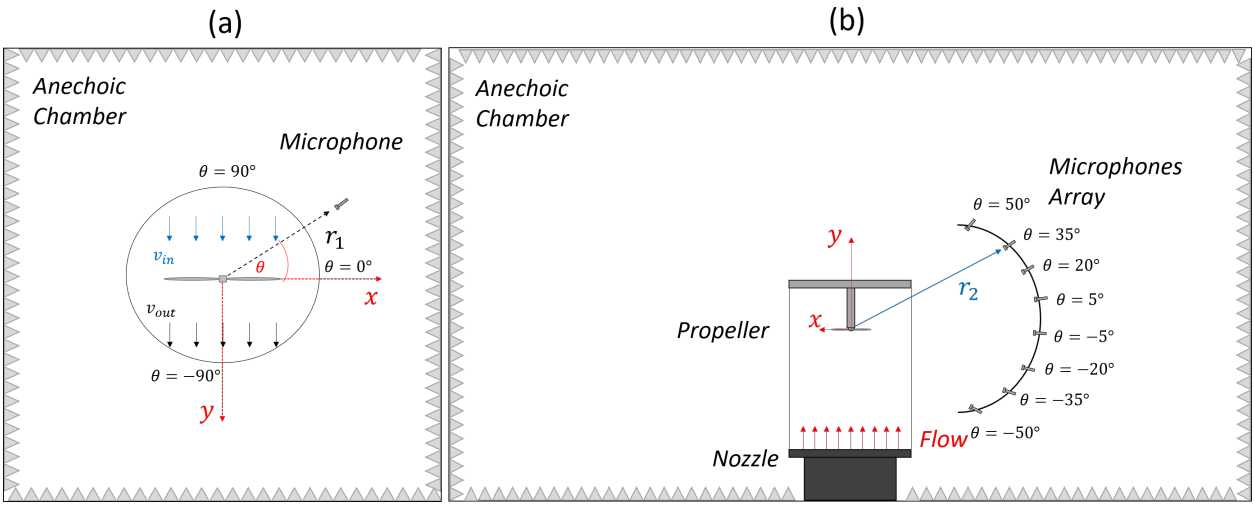

Fig. 2 Sketch of the experimental setup used for the acoustic characterization (a) and for the aerodynamic and aero-acoustic measurements campaign(b).

a US Digital EM1 transmissive optical encoder, coupled with a US Digital disk of 1 in diameter and 200 pulses per revolution. Rotor thrust is measured using a Futek LSB200 load cell excited with 5 VDC. The load cell is characterized by a maximum capacity of 22.2 N, nonlinearity and hysteresis of ± 0.1 % of RO, and an operating temperature between -50 to 90 $°C$. The torque is measured using a Transducer Techniques RTS-25 torque sensor excited with 10 VDC. It has a maximum capacity of 0.18 Nm, nonlinearity and hysteresis of ± 0.1 % of RO, and an operating temperature between -54 to 93 $°C$. The thrust and torque signals are acquired by a National Instrument acquisition board with a sampling frequency of 5 kHz and an acquisition time of 30 s.

Far-field noise measurements are performed by means of microphones mounted on a semicircular array, centered at the propeller axis, as sketched in Fig.2(b). The array has a radius of $r = 1.20\,m = 5D$ and is constituted by 4 LinearX M51 and 4 LinerarX M53 free field microphones, with a maximum SPL of 150 dB and 130 dB respectively, a diameter of 1/2 inch and a frequency range between 20 Hz and 20 kHz. The Data Acquisition System (DAS) consisted of two National Instrument modules NI9234. A polar reference system has been adopted to define the angular position of each microphone with respect to the propeller center, the reference system is defined in Fig.2(b). Pressure fluctuation time histories have been recorded for 30 s at a sampling rate of $f_s = 51200\,Hz$.

Then, a stereoscopic PIV investigation was conducted to measure the propeller flow field. Sets of 500 images have been recorded. The flow is seeded with particles of 1-micron median diameter produced by a SAFEX Twin Fog generator with SAFEX-Inside-Nebelfluid, a mixture of diethylene glycol and water. The particles are introduced in the wind tunnel circuit to ensure a uniform concentration while recirculating. Illumination of the field of view is provided by a double cavity Quantel EVerGreen EVG00200 Nd:YAG laser with 200 mJ/pulse energy. The laser sheet is aligned with the propeller axis of rotation. Two Imager sCMOS cameras with 2560x2160 pixels and four Nikon lenses with 50 mm focal length at f# 8 have been used for the measurements. In order to align the measurement plane with the focal plane, Scheimpflug adapters have been mounted on each camera. The camera calibration, acquisition, and post-processing have been carried out with the LaVision Davis 8.4 software. The images are processed with a window deformation iterative multi-grid with a final interrogation window size of 16 x 16 pixels and 50% overlap. Spurious vectors are isolated through a median filter and replaced by interpolation. Details of the PIV setup apparatus are given in Tabs.1- 2.

V. Results

The initial phase of the investigation was aimed at quantifying the serration effect on noise emissions. For this purpose, the OverAll Sound Pressure Level (*OASPL*) of each propeller was computed at various angular positions. For conciseness, only the most noteworthy findings are presented in this manuscript, specifically those corresponding to the rotor plane at a polar angle $\theta = 0°$ (refer to Fig.3(a)), and the wake region at a polar angle $\theta = 30°$ and $60°$, addressed in

Downloaded by Technische Universiteit Delft on July 17, 2024 | http://arc.aiaa.org | DOI: 10.2514/6.2024-3107

Table 1 Details of Imaging Parameters.

Imaging Parameters	
Camera	2 Imager sCMOS
Number of pixels [px]	2560 x 2160
Pixel size [μm]	6.5 x 6.5
Focal length [mm]	50
Magnification	0.05
FOV [cm^2]	35 x 35
Imaging resolution [px/mm]	8

Table 2 Details of PIV Parameters.

PIV Parameters	
Software	LaVision Davis 8.4
Pulse separation [μs]	10
Number of recordings	500
Windows size [px^2]	16 x 16

Downloaded by Technische Universiteit Delft on July 17, 2024 | http://arc.aiaa.org | DOI: 10.2514/6.2024-3107

Fig.3(b) and (c). The OASPL is defined as:

$$OASPL = 10\ \log_{10}\left(\frac{\sigma_P}{p_{ref}}\right)^2 \tag{5}$$

where the σ_P is the standard deviation of the pressure time series evaluated as:

$$\sigma_P^2 = \int_{f_1}^{f_2} PSD(f)df \tag{6}$$

Being f_1 and f_2 the boundaries of the region of interest, in the present case they are established to cover the entire microphone linear operating range, and the PSD is the Power Spectral Density of the pressure signal expressed in Pa^2/Hz. Moreover, p_{ref} is the reference pressure equal to 20 μPa (threshold of human hearing). In Fig. 3, each marker represents a propeller with a different STE geometry. Furthermore, for comparison, a red dashed line has been added to each graph, representing the baseline propeller (i.e., a propeller that has not undergone any acoustic optimization). Any data point below the red line indicates a lower noise level compared to the reference propeller. Several test cases in Fig.3(a)-(b) exhibit higher noise levels than the baseline propeller, as indicated by the markers positioned above the red line. This representation highlights the variability in acoustic emissions across different configurations. As a result, the requirement of AR_t less than 4, as suggested by Ning et al.[32, 33], does not guarantee noise reduction. The results related to the wake region, identified by $\theta = 60°$ (Fig.3(c)), show that the majority of serrated propellers exhibit a lower acoustic impact compared to the reference case. This finding suggests the existence of preferential regions where serrations prove to be effective. Notably, as one transitions from the rotor plane (Fig.3(a)) towards the wake region (Fig.3(c)), the impact of serrations becomes increasingly significant. Focusing on the wake region, the worst and the best propellers were identified and indicated by red and green circles and labeled as STE1 and STE2, respectively. Subsequently, a spectral analysis was conducted for these test cases, and the results were compared to those of the baseline propeller and reported in Fig.4(a). The spectra are presented in the normalized form of the Sound Pressure Spectrum Level (*SPSL*), that according to [34–36], is defined as:

$$SPSL = 10\,log_{10}\left(\frac{PSD\ \Delta f}{p_{ref}^2}\right) \tag{7}$$

where Δf is the frequency resolution set equal to 1 Hz. Moreover, the noise spectra are represented as a function of the Harmonics of the Blade Passing Frequency $HBPF = \frac{2\pi f}{B\Omega}$; where f is the frequency of sound emissions in Hz, B is the

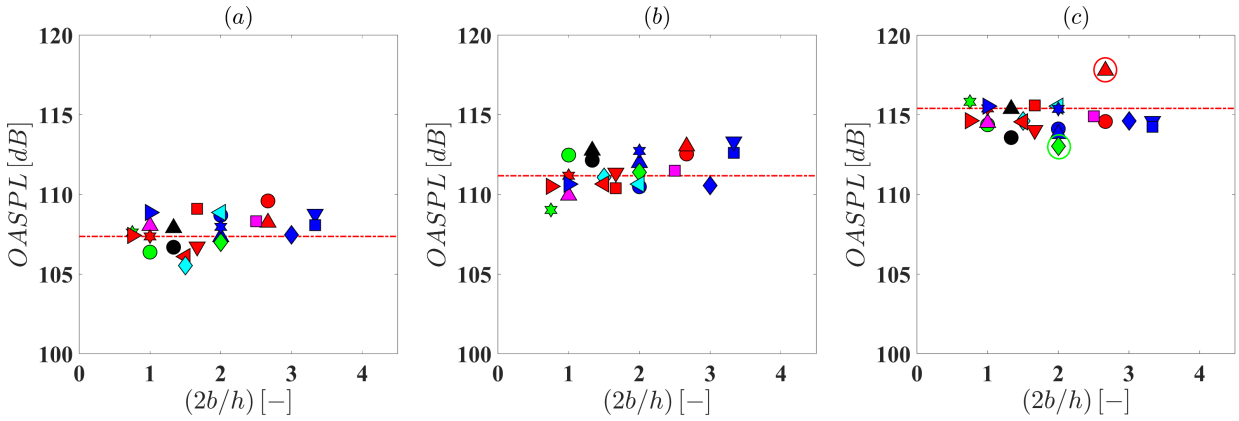

Fig. 3 OASPL measured for all the test cases at fixed rotational velocity $\Omega = 4000\,RPM$ for three polar angle stage: $\theta = 0°$(a); $\theta = 30°$(b); $\theta = 60°$(c). The red dash-dotted line represents the baseline propeller as a reference.

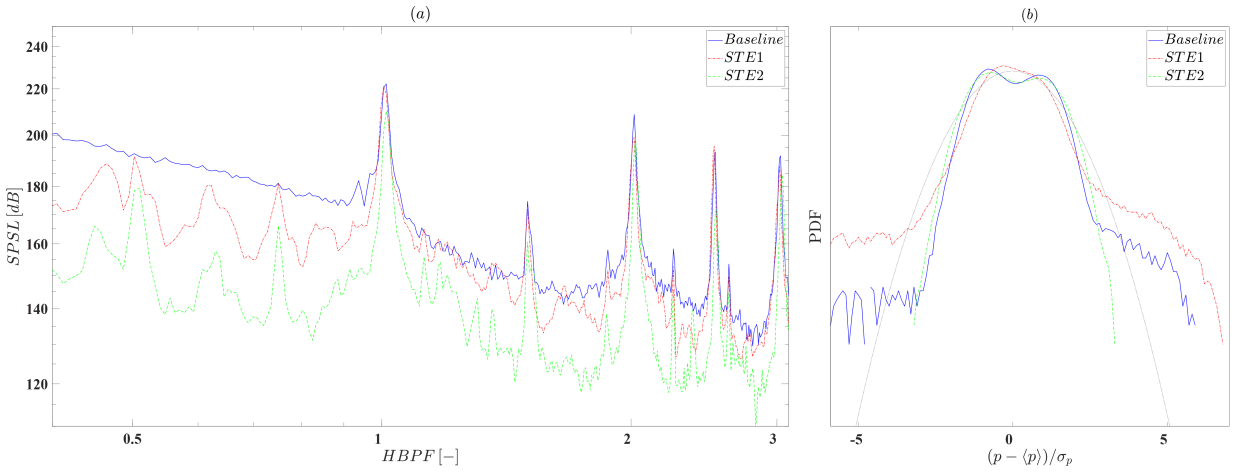

Fig. 4 Dimensionless spectra (a) and Probability Density Function (b) of the near-field pressure signals for the STE1 and the STE2 propeller at constant rotational velocity $\Omega = 4000\,RPM$ for polar angle $\theta = 60°$ in comparison with the baseline propeller.

propeller blade number and Ω is the propeller rotational velocity in $revolution/s$. The obtained results are consistent with the previous findings, providing further insights. A dual phenomenon is observed. The most significant effect is observed in the low-frequency region ($HBPF < 1$), where both STE propellers exhibit a noticeable reduction in the acoustic signature. Such results are in line with previous literature findings [6, 26, 27]. On the other hand, the STE2 propeller shows a decrease in the broadband component at all frequencies, resulting in overall mitigation in terms of $OASPL$ (as seen in Fig.3); the opposite occurs for the STE propeller. Additionally, the spectra show a reduction in the tonal component, which had not been observed previously. This result may be associated with a reduction in the thrust produced by the propeller, as the literature (see among many [6, 8, 15, 37]) states that the tonal component is primarily associated with loads along the blade. More in detail, the reference and the STE1 propeller exhibit similar intensities of tonal noise. In contrast, the STE2 configuration demonstrates a significant reduction in this component. Nevertheless, given the comparable tonal components between the STE2 and reference propellers, it can be inferred that the entirety of noise reduction cannot be solely ascribed to a reduction in thrust. Moreover, the outcomes in the low-frequency broadband region reveal that serrations effectively mitigate such components. This finding is further supported by the examination of the Probability Density Function (PDF) of the pressure time history, as reported in Fig.4(b). The variable is represented in a reduced form to achieve a zero mean and unit standard deviation. The PDFs reveal deviations from Gaussian distribution, particularly for the STE1 and baseline propellers; on the other hand, the

Downloaded by Technische Universiteit Delft on July 17, 2024 | http://arc.aiaa.org | DOI: 10.2514/6.2024-3107

STE2 propeller exhibits a reduction in the tail of the distribution. Such departures of the distribution tails are commonly related to intermittent phenomena embedded in the pressure time series that are known to contribute to broadband noise. In summary, these observations underscore the positive effects of serration in the wake region, encompassing reductions in tonal and broadband noise components, as well as the alleviation of intermittent phenomena.

Subsequently, to establish a relationship between acoustic emissions, thrust generation, and fluid-dynamic aspects, further tests were conducted using an anechoic wind tunnel. For the sake of brevity, the study focuses on the two configurations identified earlier, comparing the results with those of the reference propeller. The starting point involved quantifying the aerodynamic performance of the propellers in terms of the thrust coefficient c_T. The results are presented in Fig.5 for both the hovering condition (a) and the advanced flight condition (b). Concerning the advanced flight condition, experimental tests were conducted at a fixed propeller rotation rate of $\Omega = 5000\,RPM$. To enhance the generality of the results, the inflow velocity is expressed in dimensionless form as the Advance Ratio $J = \frac{v_\infty}{nD}$, where v_∞ is the inflow velocity, n is the rotational velocity in Hz, and D is the propeller diameter, within the range $J = [0 : 0.6]$. The thrust coefficient is defined as in [38]:

$$c_T = \frac{T}{\frac{1}{2}\rho\widehat{S}V^2} = \frac{T}{\frac{1}{2}\rho\widehat{S}(\Omega\,\frac{D}{2})^2} \tag{8}$$

T is the thrust force expressed in N, ρ the air density kept constant at $1.225\,kg/m^3$, $\widehat{S}$ is the *effective* surface of the propeller (i.e. the propeller surface taking into account the geometry modification), Ω the rotational velocity expressed in rad/s and D the propeller diameter in m. The employed formulation differs from the typical one commonly used for rotors, as discussed in various studies (e.g.,[39]). This choice was made to account for the variations in the lifting surface among the propellers, in order that the observed differences in the thrust coefficient (c_T) can be attributed to flow modifications. Fig.5 reveals a significant decrease in the c_T, particularly for the best propeller. Similar results are reported in the literature, e.g. in [6, 24, 25]. It has been demonstrated that a longer tooth length induces a greater loss of thrust. The c_T reduction involve both the hovering (Fig.5(a)) and the advanced flight conditions (Fig.5(b)). Specifically, in hovering, the decrease in c_T is less than 5% for the STE1 propeller, while it reaches 12% for the STE2 propeller. In advanced flight, the impact on thrust generation is more significant, with a reduction of 10% and 20% for the STE1 and STE2 propellers, respectively. This underscores the crucial role of well-designed serrations for mission success. Furthermore, it's essential to emphasize that to attain the same thrust as the reference propeller, an increase in engine speed may be necessary, potentially resulting in elevated drone noise production.

Moreover, regarding the results of far-field microphone measurements to maintain brevity, the manuscript focuses exclusively on the results related to hovering and advanced flight conditions at a fixed advance ratio $J = 0.36$. Initially, the OASPL was calculated at different polar angles, and the outcomes are depicted in Fig.6. The reference system is centered at the propeller hub and the polar angle is defined as illustrated in Fig.2(b). Regarding the hover condition, the results (see Fig.6(a)) reveal that the STE1 and baseline propellers have a substantially equal acoustic impact, while the STE2 propeller exhibits a noise reduction, quantified at 2 dB, concentrated in the rotor plane within a range of polar angle θ between minus 10 degrees and twenty degrees while in the other region it shows ah higher noise level than the baseline propeller. It is important to emphasize that, despite observing a thrust reduction, the STE1 propeller does not show an improvement in terms of acoustic impact. However, when analyzing the results under an advancing velocity, as depicted in Fig.3(b), what was previously mentioned is no longer valid. In this case, the main outcome is a relevant reduction of the noise level for both propellers. The mitigation ranges between 3 and 4 dB for the STE2 propeller, whereas the STE1 propeller induces an approximate reduction of 2 dB. In addition, such an effect is independent of the polar angle θ. Consequently, it can be concluded that greater tooth depth results in a more pronounced decrease in sound emissions, which correlates with a more relevant reduction in c_T. As a result, the forward flight case demonstrates a greater decrease in the thrust coefficient compared to the fixed-point flight case. However, this reduction is associated with a better acoustic gain.

Following the reasoning previously outlined, an analysis in the Fourier domain focusing on the wake region (corresponding to $\theta = 50°$) was performed, and the results are illustrated in Fig.7 for both hovering (Fig.7(a)) and advancing flight conditions (Fig.7(b)). As expected, the serrations greater influence is observed on the broadband component. Specifically, both STE propellers significantly reduce the pressure signal energy in the region of $HBPF < 1$. It is noteworthy that the STE2 propeller has also decreased the tonal component at $HBPF = 0.5$, representing engine noise. This effect can be interpreted as a reduction in blade-induced resistance. Regarding the tonal component, it can be observed that the STE1 propeller exhibits an acoustic intensity comparable to the baseline propeller, while the STE2 propeller shows a reduction. These results are more pronounced in the hover condition. In the case of advancing flight, the acoustic effects are confined to the low-frequency region, where both STE propellers exhibit a significant mitigation

Downloaded by Technische Universiteit Delft on July 17, 2024 | http://arc.aiaa.org | DOI: 10.2514/6.2024-3107

Downloaded by Technische Universiteit Delft on July 17, 2024 | http://arc.aiaa.org | DOI: 10.2514/6.2024-3107

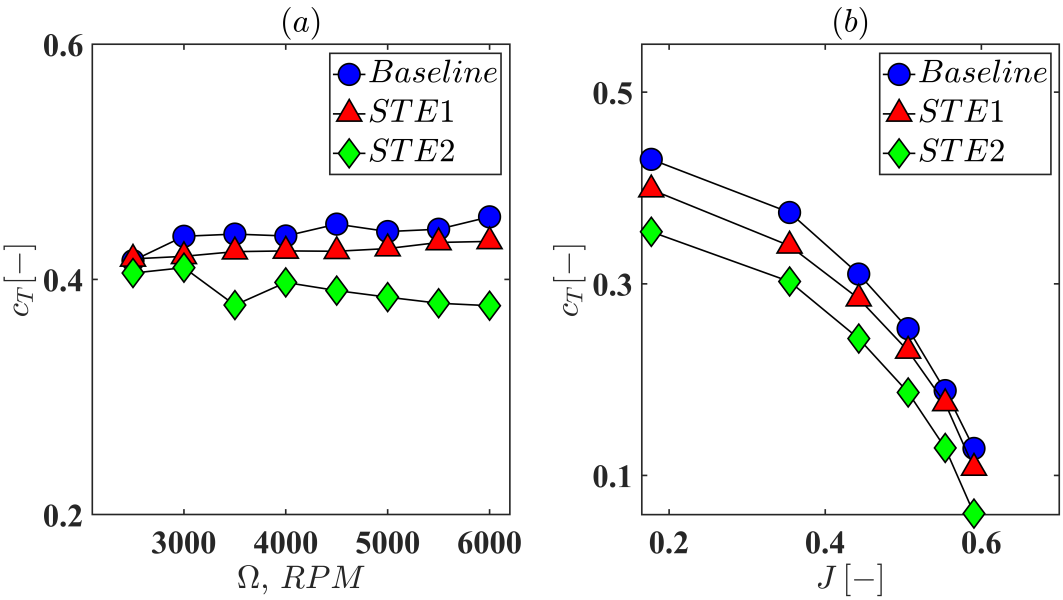

Fig. 5 Thrust coefficient c_T in hovering (a) and in advanced flight (b) conditions. The ∘ represents the baseline propeller, the △ the STE1 propeller, and the ⋄ the STE2 propeller.

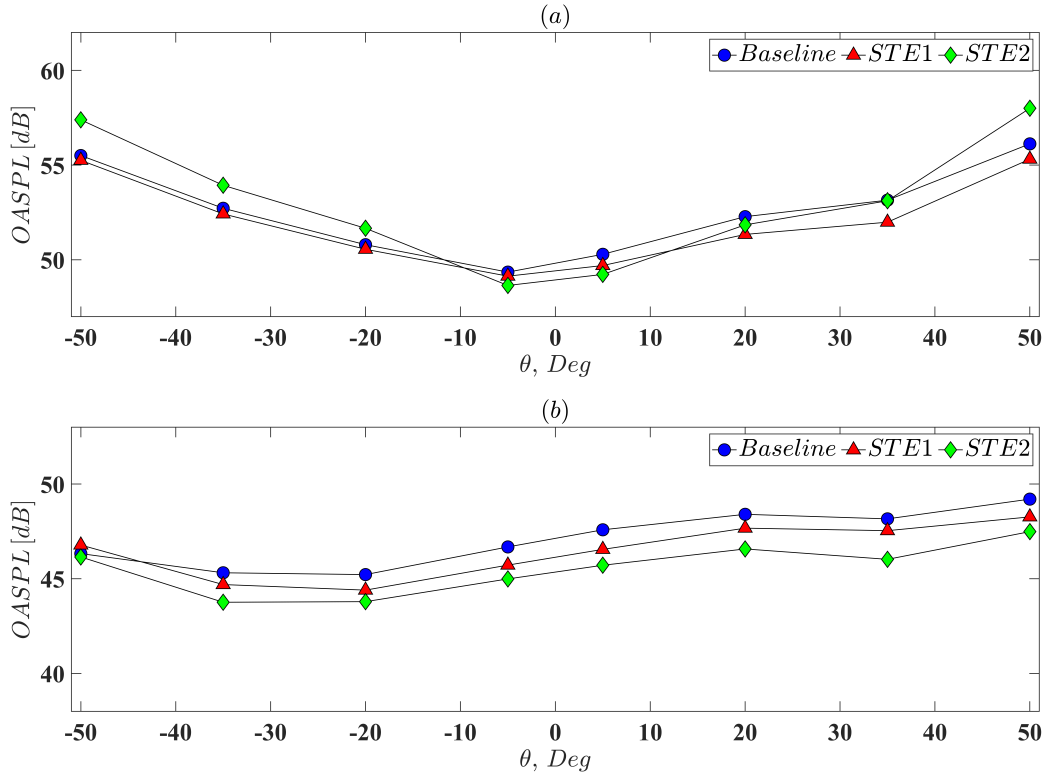

Fig. 6 OASPL measured at different polar angle θ in hovering (a) and advanced flight (b) condition. In the hovering case, the rotational velocity is fixed at $\Omega = 5000\,RPM$. On the other hand, for the advanced flight condition the inflow velocity is $V_\infty = 6\,m/s$ ($J = 0.36$) and the rotational velocity is $\Omega = 5000\,RPM$. the ∘ represents the baseline propeller, the △ the STE1 propeller and the ⋄ line the STE2 propeller.

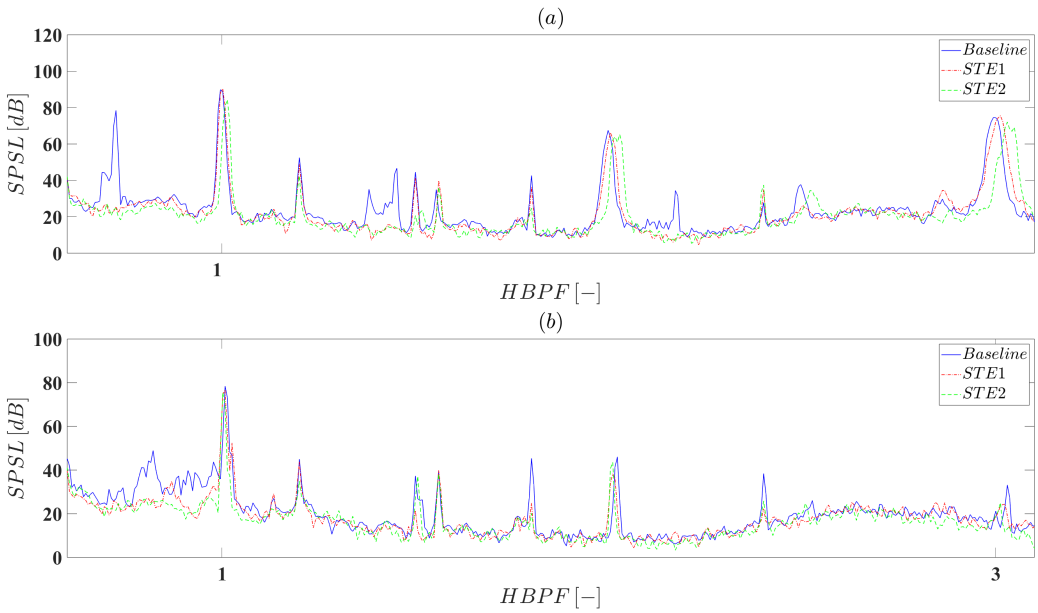

Fig. 7 Dimensionless spectra of the far-field pressure signals calculated for polar angle $\theta = -50°$ in hovering (a) and advanced flight(b) configuration. The solid blue line represents the baseline propeller, the red dash-dotted line and the green dotted line are representative of the STE1 propeller and the STE2 propeller respectively.

of sound emissions. Remarkably, in forward flight, the impact on tonal noise is less prominent than in the hovering case. In this condition, the tonal noise is buried by its broadband counterpart, which becomes more relevant.

The effect on the broadband region is further clarified through the analysis of the PDFs reported in Fig.8. The distribution functions exhibit a damping of the distribution tails in both flight conditions, although the effect is more pronounced in the advanced flight condition. During hovering flight, all three rotors exhibit a very similar behavior with a negatively skewed distribution for both the baseline propeller and the STE1 propeller. This skewness may account for the higher intensity of the broadband component in these two propellers, as observed in Fig.7(a). On the other hand, the predominant effect is noticeable during advanced flight, as depicted in Fig.8(b). In this case, the baseline propeller exhibits a deviation in the distribution tail, which is less pronounced for the STE propellers. This result validates and helps interpret the results obtained for the OASPL in Fig.6(a). In fact, it is possible to assume that such an effect is related to the mitigation of coherent structures embedded in the pressure time series, strictly connected with the vorticity shed at the trailing edge, resulting in a lower broadband noise emission. The obtained results and the literature (e.g.[8, 23, 24]) lead to the conclusion that the coherence of the vorticity structures released at the trailing edge is strongly influenced by the serrations.

To gain insights into how the serrations modify the flow around the blade and to establish a relationship with noise generation, stereoscopic PIV of the propeller slipstream was conducted at a constant rotational speed of $\Omega = 5000\ RPM$ and Advance Ratio $J = 0.36$. Fig.9 presents the average, on the first row and root mean square (rms) velocity distributions, on the second row, in the propeller slipstream with the flow aligned with the y-axis. The reference system is centered at the propeller hub, as illustrated in Fig.2(b), with the x and y axes normalized with respect to the propeller diameter. The increase of the axial velocity component downstream can be identified in all the propellers. More in detail, the baseline and STE1 propellers (Figs. 9(a)-(b)) present similar values of wake velocity whereas, the STE2 propeller shows a reduction. This aspect is more evident in Fig.10, which presents the mean velocity profiles for the three propellers at three different stations in the slipstream, respectively, $y/D = 0.2$ (a), $y/D = 0.4$ (b) and $y/D = 0.6$ (c). The STE1 propeller demonstrates almost identical maximum velocity compared to the baseline, whereas the STE2 propeller shows a reduction of approximately 20% compared to the baseline. Furthermore, the serrations also affect the distribution of induced velocity along the x-direction. The x-position of the maximum velocity for the best propeller differs from that of the worst propeller and is closer to the propeller root. Such an effect is certainly associated with the observed reduction in thrust. In addition, the rms velocity contour (second row of Fig.9) highlights that most of the velocity

Downloaded by Technische Universiteit Delft on July 17, 2024 | http://arc.aiaa.org | DOI: 10.2514/6.2024-3107

Downloaded by Technische Universiteit Delft on July 17, 2024 | http://arc.aiaa.org | DOI: 10.2514/6.2024-3107

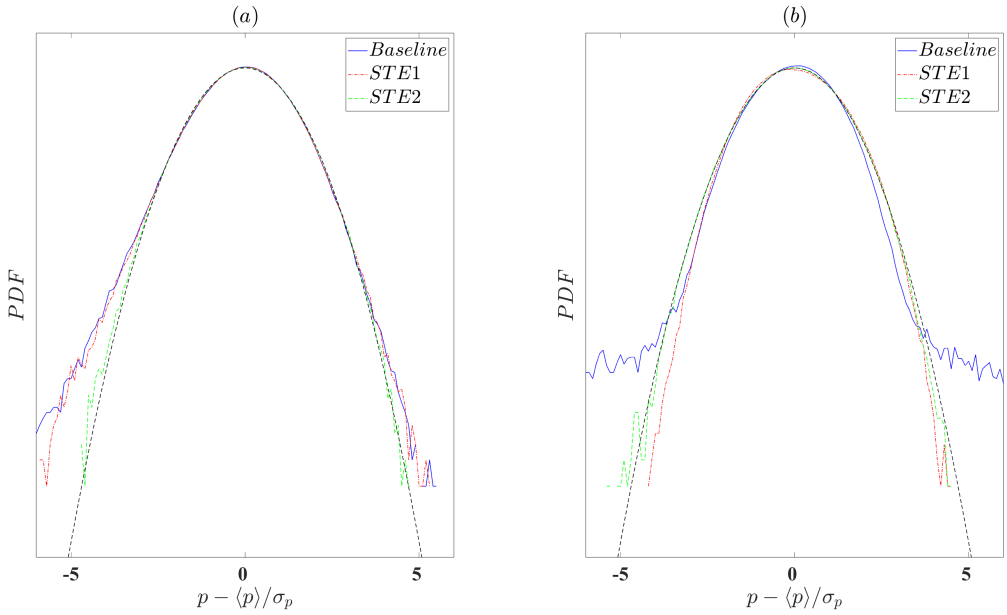

Fig. 8 Probability Density Functions of the far-field pressure signals calculated for polar angle $\theta = -50°$ in hovering (a) and advanced flight (b) configuration.

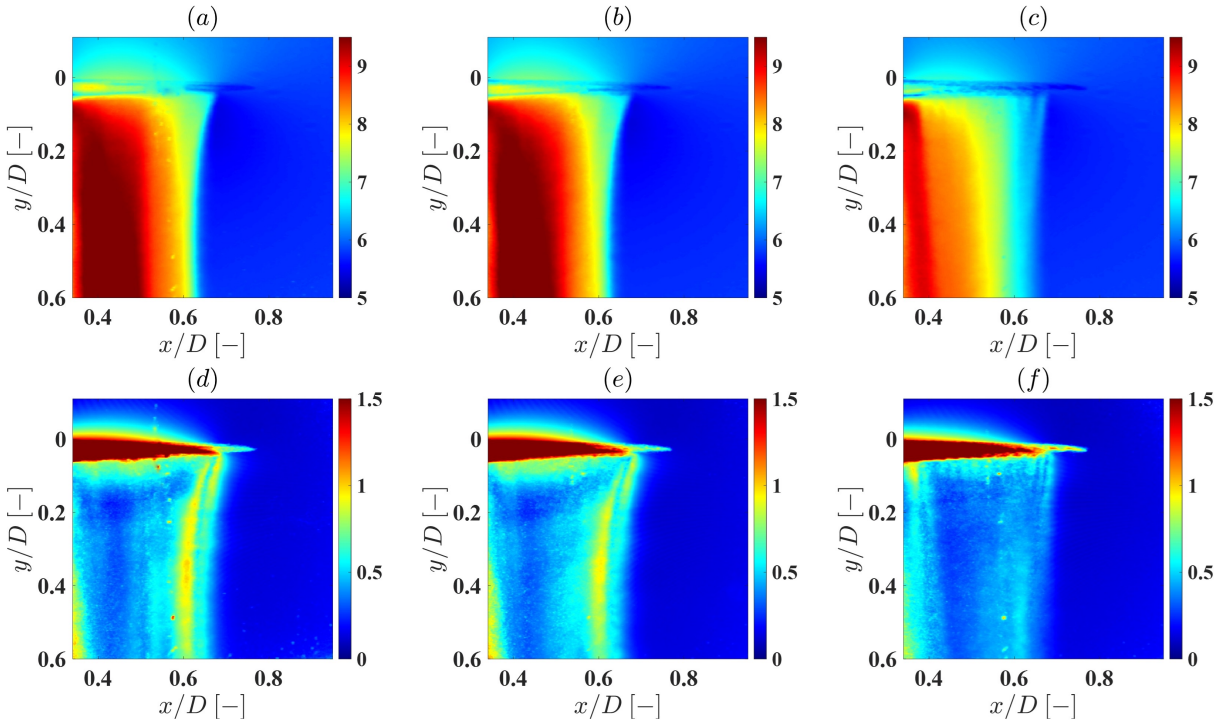

Fig. 9 Mean velocity field for the baseline propeller (a), the STE1 propeller (b) and the STE2 propeller (c) and RMS velocity field for the baseline propeller(d), the STE1 propeller (e) and the STE2 propeller(f). Contour plot obtained at fixed velocity $v_\infty = 6\,m/s$ and rotational speed $\Omega = 5000\,RPM$.

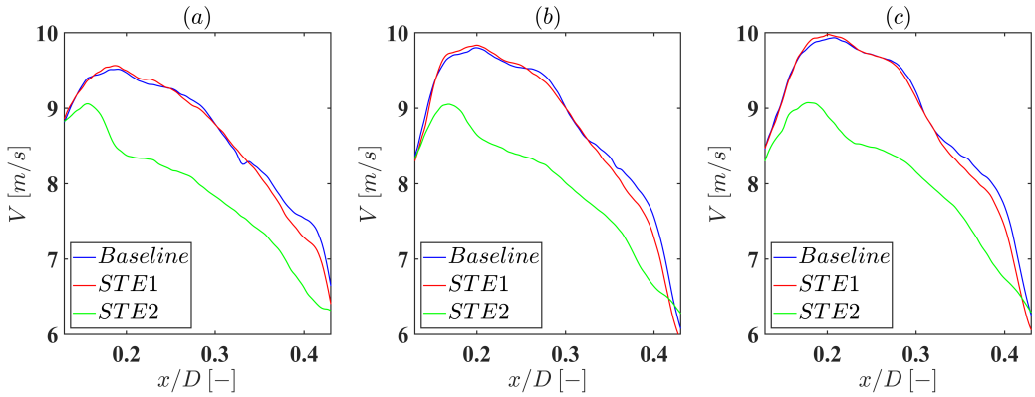

Fig. 10 Mean velocity profiles at (a) $y/D = 0.2$**, (b)** $y/D = 0.4$ **and (c)** $y/D = 0.6$ **for** $v_\infty = 6\,m/s$ **and** $\Omega = 5000\,RPM$**.**

fluctuations are associated with the generation of the tip vortices, that are shed in the wake afterward. The intensity of the tip vortex generated by the STE1 propeller (Fig.9(e)) is slightly lower compared to the baseline. Moreover, it is evident that the intensity of the tip vortex for the STE2 propeller, reported in the (f) figure, is much lower than the baseline and it is convected downstream and dissipated faster. These results confirm that the serration led to a faster dissipation and a reduced trailing edge vorticity sheet intensity.

Finally, Phase-locked (PL) PIV measurements were performed to provide further insights into how the vorticity along the blade trailing edge is shed into the wake. Fig.11 reports the rms velocity distribution corresponding to three different phases for the baseline in the first row, the STE1 in the second row and the STE2 propellers in the third row. The PL-PIV reveals that the trailing edge vorticity sheet is generated at the rotor plane in the first column, released into the wake in the second column, and travels downstream in the third column. The performance of the STE2 propeller is notable, as the distribution of rms velocity exhibits evidence of the serration pattern. This prominently indicates the disruption of spanwise correlation length, known to be associated with trailing edge noise according to Sinibaldi and Marino [8]. This outcome provides a valid explanation for the observed reduction in broadband noise. Moreover, for both STE propellers, the rms velocity along the entire blade is lower compared to the baseline configuration. Additionally, it is observed that the tip vortex is significantly less intense for the STE1 propeller compared to the baseline, whereas it becomes entirely attenuated for the STE2 propeller. Consequently, as previously documented in the scientific literature, the application of serrations at the trailing edge serves to weaken and, in certain configurations, eliminate one of the primary sources of tonal noise, thereby demonstrating the dual effect observed in the Fourier domain.

Downloaded by Technische Universiteit Delft on July 17, 2024 | http://arc.aiaa.org | DOI: 10.2514/6.2024-3107

Downloaded by Technische Universiteit Delft on July 17, 2024 | http://arc.aiaa.org | DOI: 10.2514/6.2024-3107

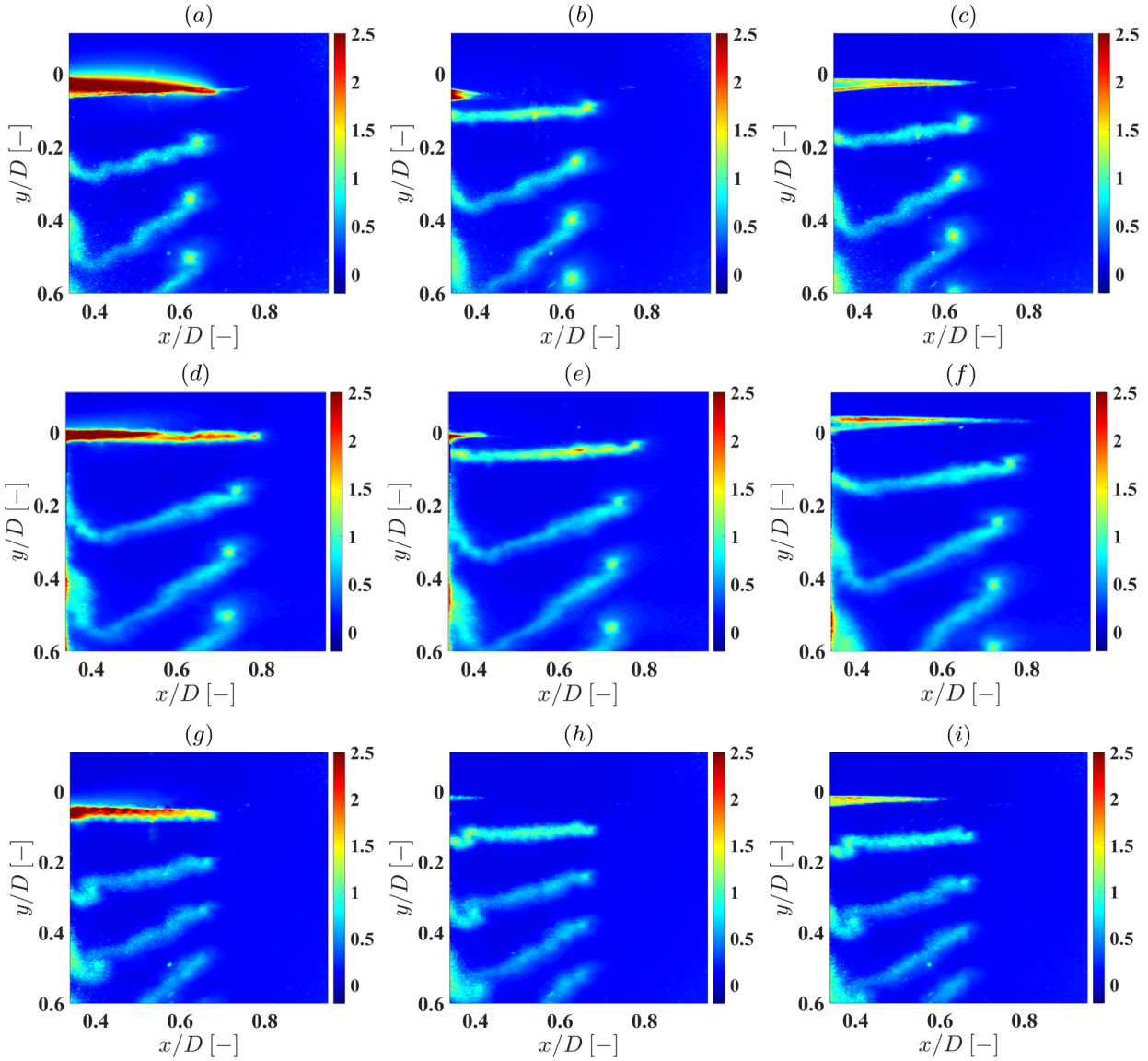

Fig. 11 Velocity rms distribution of the phase-locked PIV measurements for the baseline propeller and the STE1 and STE2 propeller at $J = 0.36$ and $\Omega = 5000\ RPM$.

Downloaded by Technische Universiteit Delft on July 17, 2024 | http://arc.aiaa.org | DOI: 10.2514/6.2024-3107

VI. Conclusion

A total of twenty-three propellers were manufactured with sawtooth pattern applied at the trailing edge, and their noise signatures were investigated. The initial phase consists of an experimental analysis to assess the tooth impact on noise emissions in hovering conditions and, in addition, to find the most interesting test cases to focus the investigation. The OASPL was employed as a metric to evaluate the noise performance. It was observed that careful attention is required during the design of STE propellers, as an improper serration design can potentially lead to an increase in propeller noise. Focusing on the wake region, the analysis in the Fourier domain of the pressure signals demonstrates that serrations induce mitigation in both the broadband and tonal noise components. The expected reduction in broadband noise aligns with previous studies in the literature. However, the effect on tonal noise has not been observed yet and opens new questions regarding the applicability of such a control strategy. In addition, the statistical analysis, in terms of Probability Density Functions, indicates a damping in the tails of the distribution function for the serrated propellers compared to the baseline. Such results motivate a deeper investigation to enhance our understanding of the problem.
This second phase aimed at examining the aerodynamic and aeroacoustic properties of STE propellers, as well as analyzing the velocity field downstream of the propeller, in forward flight conditions. The results show a reduction in the thrust coefficient, consistent with existing literature, amounting to approximately 10-15%. This result suggests that this control strategy implementation should be carefully considered and limited to specific applications where the loss in thrust does not compromise mission success. Furthermore, the far-field microphone measurements reveal a reduction of about 2 decibels in hovering for the STE2 propeller, while the STE1 propeller exhibits the same acoustic impact as the reference case in hovering. On the other hand, in advanced flight, both rotors show a noise reduction, reaching 4 decibels for the STE2 propeller. The statistical analysis once again highlights a departure from Gaussian distribution in advanced flight conditions, indicating the presence of coherent structures within the time history, damped by serrations. The mitigation of coherent structures could be the first hypothesis to interpret the mechanism underlying noise reduction. Moreover, the flow field around the blade has been characterized by means of PIV and Phase-Locked PIV measurements. The mean velocity and root main square velocity fields indicate a reduction in the wake velocity and in the tip vortex intensity. Moreover, the rms velocity field obtained by phase-locked PIV measurements shows also a lower intensity and faster dissipation of the trailing edge vorticity sheet along the entire blade. Moreover, in the rms velocity fields for the STE propellers, it is possible to observe a trace of the serration pattern. This confirms that the fluid-dynamic correlation length has been influenced by the blade's geometry, leading to a rapid dissipation of vorticity at the trailing edge, resulting in a reduced intensity of the broadband noise component.
In conclusion, the use of serration at the trailing edge as a passive control strategy to reduce the noise emission of a small drone proves to be highly promising. This approach is particularly attractive for applications that demand minimal noise impact, such as urban environments, or that prioritize reduced motion range, such as infrastructure reconnaissance or mining operations. In these scenarios, a trade-off between thrust reduction and noise reduction can be accepted, making serrations a viable solution.

Acknowledgments

References

[1] Kapustina, L., Izakova, N., Makovkina, E., and Khmelkov, M., "The global drone market: main development trends," *SHS Web of Conferences*, Vol. 129, EDP Sciences, 2021, p. 11004.

[2] Schäffer, B., Pieren, R., Heutschi, K., Wunderli, J. M., and Becker, S., "Drone Noise Emission Characteristics and Noise Effects on Humans—A Systematic Review," *Int. J. Environ. Res. Public Health*, Vol. 18, No. 11, 2021, p. 5940.

[3] FAA, "FAA Aerospace Forecast, Fiscal Years 2019–2039; Federal Aviation Administration," Tech. rep., Washington, DC, USA, 2022.

[4] Gur, O., and Rosen, A., "Optimizing Electric Propulsion Systems for Unmanned Aerial Vehicles," *J. Aircr.*, Vol. 46, No. 4, 2009, pp. 1340–1353. https://doi.org/10.2514/1.41027.

[5] Gur, O., and Rosen, A., "Design of a Quiet Propeller for an Electric Mini," *J. Propul. Power*, Vol. 25, No. 3, 2009, pp. 717–728. https://doi.org/10.2514/1.38814.

[6] Pagliaroli, T., Candeloro, P., Camussi, R., Giannini, O., R.Panciroli, and Bella, G., "Aeroacoustic Study of small scale Rotors for mini Drone Propulsion: Serrated Trailing Edge Effect." *2018 AIAA/CEAS Aeroacoustics Conference*, 2018. https://doi.org/10.2514/6.2018-3449.

[7] Pagliaroli, T., Moschetta, J., Benard, E., and Nana, C., "Noise signature of a MAV rotor in hover," *49th International Symposium of Applied Aerodynamics Lille, 24-25-26 March 2014*, 2014, pp. 24–25.

[8] Sinibaldi, G., and Marino, L., "Experimental analysis on the noise of propellers for small UAV," *Appl. Acoust.*, 2013. https://doi.org/10.1016/j.apacoust.2012.06.011.

[9] JanakiRam, D., and Scruggs, B., "Investigation of performance, noise and detectability characteristics of small-scale remotely piloted vehicle /RPV/ propellers," *7th Aeroacoustics Conference*, Vol. 19, No. 12, 1981, pp. 1052–1060. https://doi.org/doi:10.2514/6.1981-2005.

[10] Serré, R., Chapin, V., Moschetta, J.-M., and Fournier, H., "Reducing the noise of Micro-Air Vehicles in hover," *International Micro Air Vehicle Conference and Flight Competition (IMAV 2017)*, Toulouse, France, 2017, pp. 51–59. URL https://hal.science/hal-02407208.

[11] Leslie, A., Wong, K., and Auld, D., "Broadband Noise Reduction on a mini-UAV Propeller," *14th AIAA/CEAS Aeroacoustics Conference (29th AIAA Aeroacoustics Conference)*, 2008, p. 3069. https://doi.org/10.2514/6.2008-3069.

[12] Nelson, P., and Morfey, C., "Aerodynamic Sound Production," *J. Sound Vib.*, Vol. 79, No. 2, 1981, pp. 263–289. https://doi.org/10.1016/0022-460X(81)90372-2.

[13] Rozenberg, Y., Roger, M., and Moreau, S., "Rotating Blade Trailing-Edge Noise: Experimental Validation of Analytical Model," *AIAA Journal*, 2010. https://doi.org/10.2514/1.43840.

[14] Nargi, R., Candeloro, P., De Gregorio, F., Ceglia, G., and Pagliaroli, T., "Fluid-Dynamic and Aeroacoustic Characterization of Side-by-Side Rotor Interaction," *Aerospace*, Vol. 10(10), 2023, p. 851. https://doi.org/10.3390/aerospace10100851.

[15] Candeloro, P., Ragni, D., and Pagliaroli, T., "Small-Scale Rotor Aeroacoustics for Drone Propulsion: A Review of Noise Sources and Control Strategies," *Fluids*, Vol. 7, No. 8, 2022, p. 279. https://doi.org/10.3390/fluids7080279.

[16] Candeloro, P., Martellini, E., Nederlof, R., Sinnige, T., and Pagliaroli, T., "An Experimental Study of the Aeroacoustic Properties of a Propeller in Energy Harvesting Configuration," *Fluids*, Vol. 7, No. 7, 2022. https://doi.org/10.3390/fluids7070217, URL https://www.mdpi.com/2311-5521/7/7/217.

[17] Llorente, E., and Ragni, D., "Trailing-edge serrations effect on the performance of a wind turbine," *J. Renew. Energy*, Vol. 147, 2020, pp. 437–446. https://doi.org/10.1016/j.renene.2019.08.128.

[18] Oerlemans, S., Fisher, M., Maeder, T., and Kögler, K., "Reduction of Wind Turbine Noise Using Optimized," *AIAA j*, Vol. 47, No. 6, 2009. https://doi.org/10.2514/1.38888.

[19] Oerlemans, S., "Reduction of Wind Turbine Noise using Blade Trailing Edge," *22nd AIAA/CEAS Aeroacoustics Conference*, 2016, pp. 1–18. https://doi.org/10.2514/6.2016-3018.

[20] Chong, T., and Vathylakis, A., "On the aeroacoustic and flow structures developed on a flat plate with a serrated sawtooth trailing edge," *J. Sound Vib.*, 2015. https://doi.org/10.1016/j.jsv.2015.05.019.

[21] Avallone, F., Van Der Velden, W., Ragni, D., and Casalino, D., "Noise reduction mechanisms of sawtooth and combed-sawtooth trailing-edge serrations," *J. Fluid Mech.*, 2018. https://doi.org/10.1017/jfm.2018.377.

[22] Howe, M., "Noise produced by a sawtooth trailing edge," *J. Acoust. Soc. Am.*, Vol. 90, No. 1, 1991, pp. 482–487. https://doi.org/10.1121/1.401273.

[23] Pang, E., Cambray, A., Rezgui, D., Azarpeyvand, M., and Showkat-Ali, S., "Investigation Towards a Better Understanding of Noise Generation from UAV Propellers," *2018 AIAA/CEAS Aeroacoustics Conference*, 2018, p. 3450. https://doi.org/10.2514/6.2018-3450.

[24] Intravartolo, N., Sorrells, T., Ashkharian, N., and Kim, R., "Attenuation of Vortex Noise Generated by UAV Propellers at Low Reynolds Numbers," *55th AIAA Aerospace Sciences Meeting*, 2017, p. 2019. https://doi.org/10.2514/6.2017-2019.

[25] Candeloro, P., Nargi, R., Patanè, F., and Pagliaroli, T., "Experimental Analysis of Small-Scale Rotors with Serrated Trailing Edge for Quiet Drone Propulsion," *J. Phys.*, 2020. https://doi.org/10.1088/1742-6596/1589/1/012007.

[26] Halimi, A., Marinus, B., and Larbi, S., "Analytical prediction of broadband noise from mini-RPA propellers with serrated edges," *Int J Aeroacoust*, Vol. 18, No. 4-5, 2019, pp. 517–535. https://doi.org/10.1177/1475472X19859889.

Downloaded by Technische Universiteit Delft on July 17, 2024 | http://arc.aiaa.org | DOI: 10.2514/6.2024-3107

[27] Halimi, A., Marinus, B., and Larbi, S., "Trailing edge noise of innovative mini-RPA propeller blades geometry," *2018 AIAA/CEAS Aeroacoustics Conference*, 2018, pp. 1–14. https://doi.org/10.2514/6.2018-3451.

[28] Farassat, F., and Succi, G., "A review of propeller discrete frequency noise prediction technology with emphasis on two current methods for time domain calculations," *Top. Catal.*, 1980. https://doi.org/10.1016/0022-460X(80)90422-8.

[29] Schlinker, R., and Amiet, R., "Helicopter Rotor Trailing Edge Noise," *7th Aeroacoustics Conference*, 1981, p. 2001. https://doi.org/10.2514/6.1981-2001.

[30] Rozenberg, Y., Roger, M., and Moreau, S., "Fan Blade Trailing-Edge Noise Prediction Using RANS Simulations," *J. Acoust. Soc. Am.*, Vol. 123, No. 5, 2008, pp. 5207–5212. https://doi.org/10.2514/6.2010-3720.

[31] Corcos, G., "The structure of the turbulent pressure field in boundary-layer flows," *J. Fluid Mech.*, Vol. 18, No. 3, 1964, pp. 353–378. https://doi.org/10.1017/S002211206400026X.

[32] Z.Ning, and H.Hu, "An Experimental Study on the Aerodynamics and Aeroacoustic Characteristics of Small Propellers," *54th AIAA Aerospace Sciences Meeting*, 2016, p. 1785. https://doi.org/10.2514/6.2016-1785.

[33] Ning, Z., and Hu, H., "An Experimental Study on the Aerodynamic and Aeroacoustic Performances of a Bio-Inspired UAV Propeller," *35th AIAA Applied Aerodynamics Conference*, 2017, p. 3747. https://doi.org/10.2514/6.2017-3747.

[34] Pierce, A., *Acoustics: an introduction to its physical principles and applications*, Springer, 2019.

[35] Di Marco, A., Mancinelli, M., and Camussi, R., "Pressure and velocity measurements of an incompressible moderate Reynolds number jet interacting with a tangential flat plate," *J. Fluid Mech.*, Vol. 770, 2015, pp. 247–272. https://doi.org/10.1017/jfm.2015.149.

[36] Mancinelli, M., Pagliaroli, T., Di Marco, A., Camussi, R., and Castelain, T., "Wavelet decomposition of hydrodynamic and acoustic pressures in the near field of the jet," *J. Fluid Mech.*, Vol. 813, 2017, pp. 716–749. https://doi.org/10.1017/jfm.2016.869.

[37] Gur, O., and Rosen, A., "Multidisciplinary Design Optimization of a Quiet Propeller," *14th AIAA/CEAS Aeroacoustics Conference (29th AIAA Aeroacoustics Conference)*, Vol. 3073, No. May, 2008, pp. 5–7. https://doi.org/10.2514/6.2008-3073.

[38] Leishman, G., *Principles of helicopter aerodynamics with CD extra*, Cambridge university press, 2006.

[39] McCormick, B., *Aerodynamics, Aeronautics, and Flight Mechanics*, John Wiley, 1995.

Downloaded by Technische Universiteit Delft on July 17, 2024 | http://arc.aiaa.org | DOI: 10.2514/6.2024-3107